

ROM SAF Report 28

Description of wave optics modelling in ROPP-9 and suggested improvements for ROPP-9.1

S. B. Healy

ECMWF, Reading, UK

Document Author Table

| | <i>Name</i> | <i>Function</i> | <i>Date</i> | <i>Comments</i> |
|---------------------|------------------|-------------------------------|---------------|-----------------|
| Prepared by: | S. B. Healy | ROM SAF Project Team | 26 March 2018 | |
| Reviewed by: | I. D. Culverwell | ROM SAF Project Team Reviewer | 12 March 2018 | |
| Reviewed by: | K. B. Lauritsen | ROM SAF Project Manager | 20 March 2018 | |
| Approved by: | K. B. Lauritsen | ROM SAF Project Manager | 26 March 2018 | |

Document Change Record

| <i>Issue/Revision</i> | <i>Date</i> | <i>By</i> | <i>Description</i> |
|-----------------------|---------------|-----------|--|
| 0.1 | 8 March 2018 | SBH | 1st draft |
| 0.2 | 12 March 2018 | SBH | 2nd draft |
| 0.3 | 22 March 2018 | SBH | 3rd draft |
| 1.0 | 26 March 2018 | SBH | Final version, following reviews and approval. |

ROM SAF

The Radio Occultation Meteorology Satellite Application Facility (ROM SAF) is a decentralised processing centre under EUMETSAT which is responsible for operational processing of GRAS radio occultation (RO) data from the Metop satellites and RO data from other missions. The ROM SAF delivers bending angle, refractivity, temperature, pressure, and humidity profiles in near-real time and offline for NWP and climate users. The offline profiles are further processed into climate products consisting of gridded monthly zonal means of bending angle, refractivity, temperature, humidity, and geopotential heights together with error descriptions.

The ROM SAF also maintains the Radio Occultation Processing Package (ROPP) which contains software modules that will aid users wishing to process, quality-control and assimilate radio occultation data from any radio occultation mission into NWP and other models.

The ROM SAF Leading Entity is the Danish Meteorological Institute (DMI), with Cooperating Entities: i) European Centre for Medium-Range Weather Forecasts (ECMWF) in Reading, United Kingdom, ii) Institut D'Estudis Espacials de Catalunya (IEEC) in Barcelona, Spain, and iii) Met Office in Exeter, United Kingdom. To get access to our products or to read more about the project please go to: <http://www.romsaf.org>

Intellectual Property Rights

All intellectual property rights of the ROM SAF products belong to EUMETSAT. The use of these products is granted to every interested user, free of charge. If you wish to use these products, EUMETSAT's copyright credit must be shown by displaying the words "copyright (year) EUMETSAT" on each of the products used.

Abstract

The physical basis of the wave optics simulation code included in ROPP-9 is described. The ROPP wave optics simulation code is based on a multiple phase screen (MPS) approach which is well known, and so it is only reviewed briefly. A new method for computing the phase and amplitude at the LEO satellite, given the phase and amplitude at the final phase screen, is described in detail. More specifically, it is shown that the solution at the LEO can be computed efficiently in terms of standard Fresnel integrals. The simulations are tested by inverting the phase and amplitudes with a Full Spectrum Inversion (FSI) approach to produce bending angle profiles, and then comparing these with a one-dimensional geometrical optics forward model. Some errors for large bending angle cases in the lowest 2 km are identified, and improvements for implementation in ROPP-9.1 are presented.

Contents

| | | |
|----------|--|-----------|
| 1 | Introduction | 5 |
| 2 | Method | 6 |
| 2.1 | Vacuum propagation from the GNSS transmitter to the atmosphere | 6 |
| 2.2 | Multiple Phase Screen Propagation | 6 |
| 2.3 | Propagation from the final phase screen to the LEO satellite | 8 |
| 3 | Simulated examples | 11 |
| 3.1 | ROPP-9 configuration | 11 |
| 3.2 | Suggested modifications for ROPP-9.1 | 15 |
| 4 | Summary | 18 |

1 Introduction

Version 9 of the ROM SAF Radio Occultation Processing Package (ROPP-9) contains a new wave optics simulation tool. This report outlines the physical basis of the new code, and provides results from some test simulations performed with it.

The aim has been to develop a relatively simple, understandable, and adaptable wave optics simulation tool, similar to that used by Sokolovskiy for various science studies (e.g., Sokolovskiy 2001; Sokolovskiy *et al.* 2014). It is hoped that the ROPP code will enable users to investigate specific questions, such as assessing bending angle retrieval accuracy. In addition, the code may also become useful in the development of new forward models, for example as a baseline for the investigation of current ROPP forward model errors. This ROPP code is not yet designed for full, end-to-end simulations of real measurements, and the more sophisticated and general “WOP code”, developed by Michael Gorbunov (e.g., see Gorbunov (2011), available via the EUMETSAT website), is recommended by the ROM SAF for those activities. However, the ROPP implementation will be developed further in future ROPP releases, and it should be noted that many of the component subroutines are quite general, and can be modified by the user and used individually in more specific and sophisticated problems. We also note that much of the complexity of the more sophisticated codes is related to effectively mapping the general problem into the idealised geometry assumed here.

The main routine of the simulation code is based on a standard implementation of the Multiple Phase Screen (MPS) approach, which is well known and has been described in detail elsewhere (Karayel and Hinson, 1997; Sokolovskiy, 2001). However, we have derived a new approach to compute the phase and amplitude at the LEO trajectory, based on some standard approximations used in optics (Goodman, 1996). This calculation is described in detail here, and end-to-end results using a simplified implementation of the Full Spectrum Inversion (FSI, Jensen *et al.*, 2003) approach are presented. Simulation errors are shown for some challenging cases with large bending angle fluctuations in the lowest 2 km. Unfortunately, the errors in these cases are caused by the propagation from the final screen to the LEO with the new approach used in ROPP-9. New results with a slightly modified, more accurate solution for the propagation from the final screen to the LEO satellite, for implementation in ROPP-9.1, are given.

2 Method

The basic geometry of the wave optics simulation is shown in Figure 2.1. It is convenient to use a two-dimensional (x, y) Cartesian geometry, and the problem can be split into three distinct parts. Firstly, the signal is propagated assuming a vacuum from the GNSS transmitter to the edge of the neutral atmosphere, denoted in Figure 2.1 by the “First phase screen”. The wave optics propagation through the neutral atmosphere is then computed with a Multiple Phase Screen (MPS) approach (Karayel and Hinson, 1997; Sokolovskiy, 2001). Finally, the complex signal at the final phase screen is propagated to the LEO trajectory assuming propagation in vacuum.

2.1 Vacuum propagation from the GNSS transmitter to the atmosphere

Computing the complex amplitude at position (x, y) on the first phase screen, at the edge of the neutral atmosphere, is straightforward and it is given by,

$$\mathbf{U}(x, y) = \frac{A \exp [ikd_{(x,y)}]}{d_{(x,y)}} \quad (2.1)$$

where k is the wavenumber of the GNSS signal, $d_{(x,y)}$ is distance between the GNSS transmitter and the point on the first screen, and A is a factor that ensures the amplitude is unity at a height of 80 km on the first screen. Note that Sokolovskiy (2001) often assumes a plane wave at the first screen, which is only strictly valid for a transmitter at infinity, but nevertheless produces physically reasonable results.

2.2 Multiple Phase Screen Propagation

Multiple phase screen (MPS) propagation is a standard wave optics propagation approach, and it is described by, for example, Karayel and Hinson (1997) and Sokolovskiy (2001). It is straightforward to implement, as it is essentially a sequence of fast Fourier transform (FFT) calculations.

Consider the Cartesian (x, y) grid, where the signal is primarily propagating in the positive x direction (horizontal). A series of n_x screens parallel to the y axis are defined, with a fixed spacing between screens of $x_{i+1} - x_i = \Delta x$.

Each vertical screen is split into n_y vertical samples with a fixed separation, Δy . For convenience, n_y is often set to a power of 2, to enable simple FFT implementations to be used in the code.

The *complex signal*, \mathbf{U} , is stored at each of the n_y positions on a screen. The MPS approach enables the computation of the wave field at x_{i+1} given the wave field at x_i . Firstly, we compute the Fourier transform of $\mathbf{U}(y, x_i)$ in the y direction, to represent the signal at x_i as a spectrum of plane waves,

$$u(k_y, x_i) = \int_{-\infty}^{\infty} \mathbf{U}(y, x_i) \exp(-ik_y y) dy. \quad (2.2)$$

For example, the m th spatial frequency is $k_y^m = \sqrt{k^2 - (2\pi m / (n_y \Delta y))^2}$, with a range $(-n_y/2 \leq m \leq n_y/2)$. Each spatial frequency in this spectrum is then propagated individually, because the distance

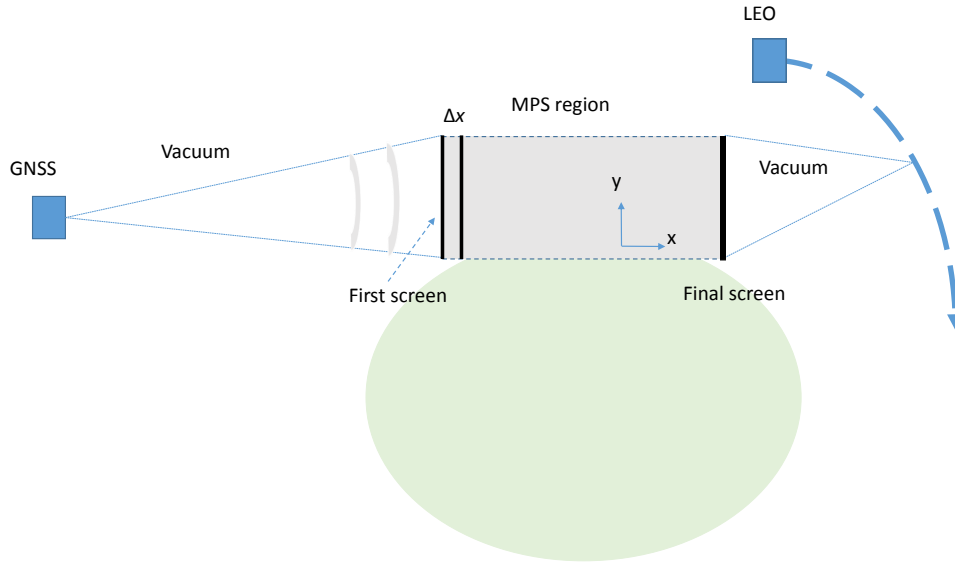


Figure 2.1: The geometry of the wave optics simulation. The GNSS signal propagates through a vacuum to the first phase screen. The propagation through the atmosphere, between the first and final screens, is performed with an multiple phase screen (MPS) approach. Vacuum propagation is assumed between the final screen and the LEO trajectory.

traveled between the screens will depend on the direction of the signal,

$$u(k_y^m, x_{i+1}) = u(k_y^m, x_i) \exp(ik_y^m \Delta x) \quad (2.3)$$

We then Fourier transform the signal back to phase and amplitude,

$$\mathbf{U}(y, x_{i+1}) = \frac{1}{2\pi} \int_{-\infty}^{\infty} u(k_y, x_{i+1}) \exp(ik_y y) dk_y \quad (2.4)$$

We then have to account for the differential delays associated with variation of the refractive index in the y direction. This is done by introducing a phase delay that depends on y , using the model refractivity, $N(x_{i+1}, y)$,

$$\mathbf{U}(y, x_{i+1}) \rightarrow \mathbf{U}(y, x_{i+1}) \exp(ik\phi(y)) \quad (2.5)$$

where,

$$\phi(y) = 10^{-6} N(x_{i+1}, y) \Delta x. \quad (2.6)$$

The MPS code in ROPP-9 does not produce reflected signals, so it is necessary to introduce a “window function” to damp the signal below the surface of the Earth (See Eq. 5, Sokolovskiy (2001), and the related discussion). This step seems somewhat arbitrary, but it is designed to remove unphysical diffraction effects associated with an artificially sharp boundary between the atmosphere and the earth’s surface used in the simulation. It also ensures that signals near the top of the vertical domain, y , are not aliased into erroneous signals near the bottom by the FFT, as a result of the FFT assuming a periodic function. The windowing is achieved by a smooth reduction of the computed signal at each screen, \mathbf{U} , to zero towards the top and bottom of the vertical domain, using a Gaussian function. The signal is reduced above a height of 120 km and below 1 km in the current ROPP-9 implementation (Sokolovskiy, 2001).

Note that if the LEO trajectory is assumed to be a straight line, parallel to the y axis, then MPS routine can be used to estimate the complex field at the LEO satellite directly. This approximation is

often acceptable in science studies (e.g. Karayel and Hinson (1987); Sokolovskiy (2001); Sokolovskiy *et al.* (2014)). However, if the LEO trajectory is not a straight line, a diffraction integral must be solved for each of the LEO positions.

2.3 Propagation from the final phase screen to the LEO satellite

We need to compute the complex signal, \mathbf{U} , at a set of receiver locations given the complex signal at the final phase screen, $\mathbf{U}_f(x_f, y)$. Consider a LEO satellite at (x_r, y_r) , measuring a complex signal $\mathbf{U}(x_r, y_r)$. For notational convenience the horizontal position of the final screen, x_f , can be set to zero and it can be omitted from the mathematics. The signal at the receiver can be evaluated by integrating,

$$\mathbf{U}(x_r, y_r) = \frac{1}{\sqrt{\lambda}} \int_y \mathbf{U}_f(y) \frac{\cos \phi}{\sqrt{r}} \exp(ikr - i\pi/4) dy \quad (2.7)$$

where the integration is performed over the entire final screen in the y direction (e.g. see Eq. 4, Gorbunov and Lauritsen, 2007). The distance between a point on the final phase screen and the receiver is $r = (x_r^2 + (y - y_r)^2)^{1/2}$, and $\cos \phi = x_r/r$ is the obliquity (or inclination) factor. The $-i\pi/4$ factor in the exponent arises as a result of mapping the 2D problem to 1D, and effectively integrating out the direction perpendicular to both x and y at the final screen. However, it is of no physical significance in this problem, because it is not a function of the receiver position.

The direct numerical integration of Eq. 2.7 can be time consuming. Gorbunov and Lauritsen (2007) have suggested a fast Fourier transform (FFT) approach, requiring a series of co-ordinate transforms. Gorbunov and Lauritsen (2007) developed their method in the context of simulating LEO-LEO measurements, where high vertical resolution is required, and the wave optics code must be fast. Their approach is efficient but it is mathematically complex. Alternatively, we suggest a new approximation of Eq. 2.7. Whilst the new approach requires some mathematical manipulations – as shown below – it is based on standard approximations used in optics. (See for example, section 4.2, Goodman, 1996.) It results in a relatively simple solution, based on summing standard integrals that arise naturally in diffraction theory.

Since the propagation is primarily in the x direction, we can assume that the angle ϕ is small and approximate,

$$\frac{\cos \phi}{\sqrt{r}} = \frac{x_r}{r^{3/2}} \simeq \frac{1}{\sqrt{x_r}}. \quad (2.8)$$

This approximation produces an error less than 1 % for a large ray bending of $\phi = 0.1$ radians. More generally, the fractional error introduced by this approximation is $\simeq 3\phi^2/4$. A second order approximation for r is used in the exponent of Eq. 2.7,

$$r \simeq x_r + \frac{(y - y_r)^2}{2x_r}. \quad (2.9)$$

Note that the validity of assuming Eq. 2.9 will be considered in section 3.2, where it will be shown that it can introduce errors in some large bending angle cases close to the surface.

Using Eq. 2.8 and Eq. 2.9, Eq. 2.7 can be approximated with,

$$\mathbf{U}(x_r, y_r) = \frac{\exp(ikx_r - i\pi/4)}{\sqrt{\lambda x_r}} \int_y \mathbf{U}_f(y) \exp\left(i \frac{k}{2x_r} (y - y_r)^2\right) dy. \quad (2.10)$$

When dealing with integrals of this form, it is useful to introduce the Fresnel integrals, $(C(x), S(x))$,

which are defined as (See section 7.3, Abramowitz and Stegun, 1972),

$$\begin{aligned} \int_0^x \exp\left(\frac{i\pi}{2}t^2\right) dt &= C(x) + iS(x) \\ S(x) &= \int_0^x \sin\left(\frac{\pi}{2}t^2\right) dt \\ C(x) &= \int_0^x \cos\left(\frac{\pi}{2}t^2\right) dt. \end{aligned} \quad (2.11)$$

The $(C(x), S(x))$ integrals can be coded up and computed efficiently using rational polynomial approximations (Heald, 1985).

Noting that $S(\infty) = C(\infty) = 1/2$ and $S(-\infty) = C(-\infty) = -1/2$, and assuming a plane wave propagating in the x direction at the final screen, $\mathbf{U}_f(y) = C$, it can be shown that Eq. 2.10 produces the expected result, $\mathbf{U}(x_r, y_r) = C \exp(ikx_r)$. More generally, consider the contribution to $\mathbf{U}(x_r, y_r)$ from a vertical interval on the final screen between $y_1 \leq y \leq y_2$. The complex signal in this interval can be written as, $\mathbf{U}_f(y) = a(y) \exp(i\psi(y))$, where a is the amplitude (real) and ψ is the accumulated phase. This is approximated assuming that both the amplitude and accumulated phase vary linearly across the vertical interval,

$$\mathbf{U}_f(y) = (a_1 + \dot{a}(y - y_1)) \exp(i\psi_1 + i\dot{\psi}(y - y_1)) \quad (2.12)$$

where ψ_1 and a_1 and are the phase and amplitude at y_1 , respectively, and the notation \dot{u} represents the derivative of u with respect to y . The parameters (a_1, \dot{a}) and $(\psi_1, \dot{\psi})$ are found by a least squares fit to the amplitude and accumulated phase values within the vertical interval.

This expression can be written in terms of $(y - y_r)$,

$$\mathbf{U}_f(y) = (a_1 + \dot{a}(y - y_r) + \dot{a}(y_r - y_1)) \exp(i\psi_1 + i\dot{\psi}(y - y_r) + i\dot{\psi}(y_r - y_1)) \quad (2.13)$$

and then introduced into Eq. 2.10

$$\begin{aligned} \delta\mathbf{U}(x_r, y_r) &= \frac{\exp(ikx_r - i\pi/4 + i\psi_1)}{\sqrt{\lambda x_r}} \int_{y_1}^{y_2} (a_1 + \dot{a}(y_r - y_1) + \dot{a}(y - y_r)) \\ &\quad \exp\left(i\frac{k}{2x_r}(y - y_r)^2 + i\dot{\psi}(y - y_r) + i\dot{\psi}(y_r - y_1)\right) dy. \end{aligned} \quad (2.14)$$

The exponent can be factored by using $ux^2 + 2vx + w = ((ux + v)^2 + wu - v^2)/u$. Hence,

$$\begin{aligned} \exp\left(i\frac{k}{2x_r}(y - y_r)^2 + i\dot{\psi}(y - y_r) + i\dot{\psi}(y_r - y_1)\right) &= \\ \exp\left(i\dot{\psi}(y_r - y_1) - i\frac{\dot{\psi}^2 x_r}{2k}\right) \times \exp\left(i\frac{2x_r}{k}\left(\frac{k}{2x_r}(y - y_r) + \dot{\psi}/2\right)^2\right). \end{aligned} \quad (2.15)$$

Let,

$$F = \frac{\exp\left(i\left(kx_r - \pi/4 + \psi_1 + \dot{\psi}(y_r - y_1) - \dot{\psi}^2 x_r/(2k)\right)\right)}{\sqrt{\lambda x_r}} \quad (2.16)$$

and use Eq. 2.15 to write Eq. 2.14 as,

$$\begin{aligned} \delta\mathbf{U} &= F \int_{y_1}^{y_2} (a_1 + \dot{a}(y_r - y_1) + \dot{a}(y - y_r)) \exp\left(i\frac{2x_r}{k}\left(\frac{k}{2x_r}(y - y_r) + \dot{\psi}/2\right)^2\right) dy \\ &= F \int_{y_1}^{y_2} \left(a_1 + \dot{a}(y_r - y_1) - \frac{\dot{a}\dot{\psi}x_r}{k} + \frac{\dot{a}2x_r}{k}\left(\frac{k}{2x_r}(y - y_r) + \dot{\psi}/2\right)\right) \\ &\quad \times \exp\left(i\frac{2x_r}{k}\left(\frac{k}{2x_r}(y - y_r) + \dot{\psi}/2\right)^2\right) dy \end{aligned} \quad (2.17)$$

This integral can be split into two parts, $\delta\mathbf{U} = \delta\mathbf{U}_1 + \delta\mathbf{U}_2$.

$$\delta\mathbf{U}_1 = F \left(a_1 + \dot{a}(y_r - y_1) - \frac{\dot{a}\psi x_r}{k} \right) \int_{y_1}^{y_2} \exp \left(i \frac{2x_r}{k} \left(\frac{k}{2x_r}(y - y_r) + \psi/2 \right)^2 \right) dy \quad (2.18)$$

This is a standard Fresnel integral (Eq. 2.11). Define,

$$\begin{aligned} I_1 &= \int_{y_1}^{y_2} \exp \left(i \frac{2x_r}{k} \left(\frac{k}{2x_r}(y - y_r) + \psi/2 \right)^2 \right) dy \\ &= \sqrt{\frac{x_r \pi}{k}} \left[C \left(2 \sqrt{\frac{x_r}{\pi k}} \left(\frac{k}{2x_r}(y - y_r) + \psi/2 \right) \right) + iS \left(2 \sqrt{\frac{x_r}{\pi k}} \left(\frac{k}{2x_r}(y - y_r) + \psi/2 \right) \right) \right]_{y_1}^{y_2} \end{aligned} \quad (2.19)$$

using integrals 7.4.38 and 7.4.39 in Abramowitz and Stegun (1972). Hence we can write,

$$\delta\mathbf{U}_1 = F \left(a_1 + \dot{a}(y_r - y_1) - \frac{\dot{a}\psi x_r}{k} \right) I_1. \quad (2.20)$$

The second term is given by,

$$\delta\mathbf{U}_2 = \frac{F \dot{a} x_r}{k} \int_{y_1}^{y_2} 2 \left(\frac{k}{2x_r}(y - y_r) + \psi/2 \right) \exp \left(i \frac{2x_r}{k} \left(\frac{k}{2x_r}(y - y_r) + \psi/2 \right)^2 \right) dy. \quad (2.21)$$

This integration is much simpler after noting the substitution,

$$V = \frac{2x_r}{k} \left(\frac{k}{2x_r}(y - y_r) + \psi/2 \right)^2. \quad (2.22)$$

The integral is given by,

$$\begin{aligned} I_2 &= \int_{y_1}^{y_2} 2 \left(\frac{k}{2x_r}(y - y_r) + \psi/2 \right) \exp \left(i \frac{2x_r}{k} \left(\frac{k}{2x_r}(y - y_r) + \psi/2 \right)^2 \right) dy \\ &= \left[\sin \left(\frac{2x_r}{k} \left(\frac{k}{2x_r}(y - y_r) + \psi/2 \right)^2 \right) - i \cos \left(\frac{2x_r}{k} \left(\frac{k}{2x_r}(y - y_r) + \psi/2 \right)^2 \right) \right]_{y_1}^{y_2} \end{aligned} \quad (2.23)$$

Using Eq. 2.19 and Eq. 2.23, the total contribution from vertical interval ($y_1 \leq y \leq y_2$), can be written as,

$$\delta\mathbf{U} = F \left[\left(a_1 + \dot{a}(y_r - y_1) - \frac{\dot{a}\psi x_r}{k} \right) I_1 + \frac{\dot{a} x_r}{k} I_2 \right] \quad (2.24)$$

The total signal at the LEO satellite is then computed by summing the contributions from the “ j ” vertical intervals, $\mathbf{U}(x_r, y_r) = \sum_j \delta\mathbf{U}_j$.

3 Simulated examples

3.1 ROPP-9 configuration

The wave optics code has been tested with a 55 refractivity profile dataset derived from ECMWF forecasts, which is now routinely used by ESA. This dataset is available from the ROM SAF web-pages. For access to this data see “*NWP model refractivity profile dataset generated in EUMETSAT Study, Aug. 29, 2017*”,

http://www.romsaf.org/previous_news.php.

All 55 cases have been processed successfully during testing, but only 4 cases will be presented here (See Table 3.1). The dataset was originally designed to provide a range of simulation conditions, and it is split into four categories, based on the maximum refractivity gradient above 100 m. The four categories are:

- **Category 1** (Standard): The maximum refractivity gradient above 100 m is less than half that required for ducting ($(-dN/dz \leq 0.157/2$ (N units m^{-1}))
- **Category 2** (Intermediate): The maximum refractivity gradient above 100 m is $0.157/2 < (-dN/dr \leq 0.1$ (N units m^{-1}))
- **Category 3** (Challenging): The maximum refractivity gradient above 100 m is $0.1 < (-dN/dr \leq 0.157$ (N units m^{-1}))
- **Category 4** (Elevated Duct): The maximum refractivity gradient above 100 m is $(-dN/dr > 0.157$ (N units m^{-1}))

We present one case from each category. The refractivity profiles, $N(r)$, are given on 91 height levels from the surface to ~ 80 km. The wave optics computation of amplitudes requires refractivity gradients that are continuous across the model level boundaries. To achieve this, we fit a cubic spline to the log of the refractivity profile, $\ln(N(r))$. The cubic spline routines used in the wave optics code are based on the section 3.3 of Press *et al.* (1992).

The simulation geometry is for a setting occultation. A stationary GPS satellite is at an altitude of 2×10^4 km. The LEO satellite is at an altitude of 800 km, with a circular orbit and an angular velocity $\dot{\theta} = 1.036 \times 10^{-3}$ rads $^{-1}$. The LEO measures the complex wave field 20000 times at a frequency of 200 Hz, spanning a vertical interval from a straight line tangent altitude (SLTA) of 80 km down to a SLTA of -300 km.

| Category | Date | Time (UTC) | lat (deg) | lon (deg) | Name |
|----------|----------|------------|-----------|-----------|---------|
| 1 | 20100916 | 12:46:40 | 20.72 | -56.80 | CASE_51 |
| 2 | 20100701 | 12:16:07 | 21.40 | 121.10 | CASE_07 |
| 3 | 20100701 | 23:53:17 | -6.37 | -85.90 | CASE_12 |
| 4 | 20100701 | 11:59:02 | -29.06 | -75.84 | CASE_05 |

Table 3.1: The refractivity profiles used in the wave optics testing.

We use $n_x = 401$ MPS screens in the horizontal separated by 5 km, spanning 2000 km in total. Each MPS screen is composed of $n_y = 2^{19}$ points separated by 1 m, spanning 524.288 km in the vertical. The lowest point on the screen is 300 km below the surface. The vertical interval on the final phase screen – used to fit the phase and amplitude parameters in Eq. 2.12 and the subsequent integrations – is 32 m.

The assumption of a stationary GNSS satellite and a circular LEO orbit means that the the phase and amplitude can be inverted with a relatively simple implementation of the Full Spectrum Inversion (FSI) technique (Jensen *et al.*, 2003), which is included in ROPP. The bending angles produced with the FSI routine can be compared with bending angles computed with a one-dimensional, geometrical optics approach which provides bending angles on a 10 m impact height grid. We have used the ROPP 1D bending angle forward model for this calculation, but we have interpolated the 91 model refractivity levels to higher vertical sampling ($= 20 \times 91$), using the cubic spline fit to the $\ln(N(r))$ used in the wave optics simulation. In addition, the maximum vertical refractivity limit – required for assimilation with the 1D operator – has been removed. However, we do not simulate bending angles below a ducting layer.

The FSI amplitude provides a quality indicator, and we do not show bending angles if the amplitude of the Fourier transformed signal is below 1 % of the maximum FSI amplitude value. The FSI provides bending angles on an impact height grid with ~ 1 m vertical spacing, but these are smoothed with a Gaussian filter. More precisely, the smoothed FSI bending angles shown in the plots are given by,

$$\alpha_s(a) = \frac{1}{b} \sum \alpha(a_i) \exp(-((a - a_i)/2H)^2) \quad (3.1)$$

where the Gaussian width is $H = 5$ m, and b is a normalisation constant given by the sum of the Gaussian weighting factors.

Figures 3.1 to 3.4 show the comparison of the bending angles computed wave optics propagator and FSI inversion, with the bending angles computed directly from the interpolated refractivity profile using the ROPP 1D geometrical optics forward model. The figures show the lowest 4 km, where the bending angle characteristics can be complex and the simulations are most challenging. The category 1 bending angle profile is relatively smooth, the category 2 and 3 profiles contain more vertical structure, and the bending angle is lost near 2.7 km in the category 4 (ducting) case. The agreement between the geometrical optics and wave optics calculations is reasonably good in terms of reproducing the main features in all cases. However, in Figure 3.2, the sharp bending angle feature just below 3 km is slightly misplaced in the vertical. Further, in the category 3 example (Figure 3.3) the wave optics simulation correctly reproduces the sharp change in bending angle near 3.5 km, but it fails to produce the large bending angles greater than 0.06 rad near 3.4 km. In addition, the wave-like structure below 3 km is slightly misplaced in the vertical. It was originally assumed that these differences were primarily caused by the 1D geometrical optics forward model producing features that were difficult to measure in practice, because it did not take account of atmospheric defocusing and the real signal dynamics at the receiver. It should be also noted that a bending angle of 0.07 rad is extremely rare in BUFR files used in the assimilation of the GPS-RO data. However, more recent testing, and access to wave optics simulations provided by Joel Rasch (Joel Rasch, pers.comm. 2018) which reproduced the large bending angles in Figure 3.3 more accurately, have led to an improvement in the wave optics simulation, which will be included in ROPP-9.1.

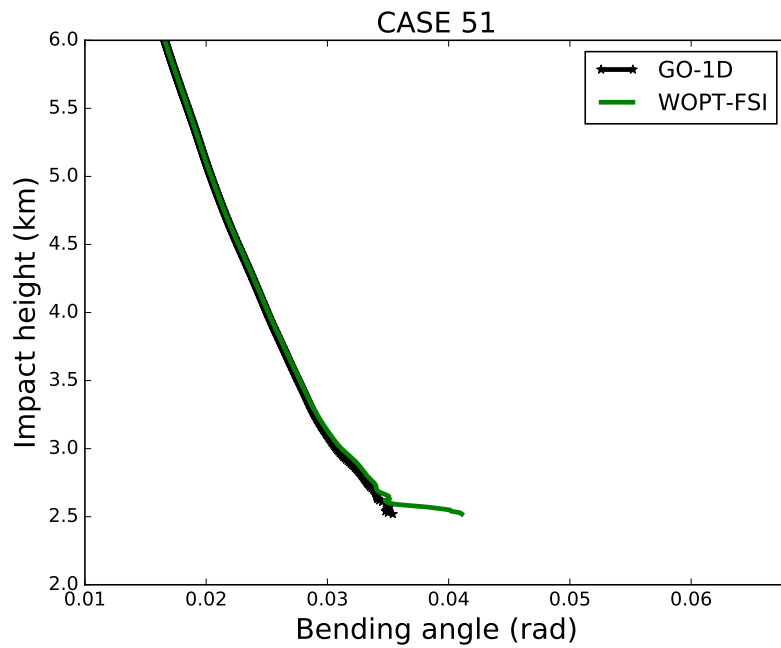


Figure 3.1: The retrieved bending angles produced with the wave optics propagator and FSI inverse (green line) and the a one-dimensional geometrical optics simulation (black line) for the category 1 profile. See table 3.1.

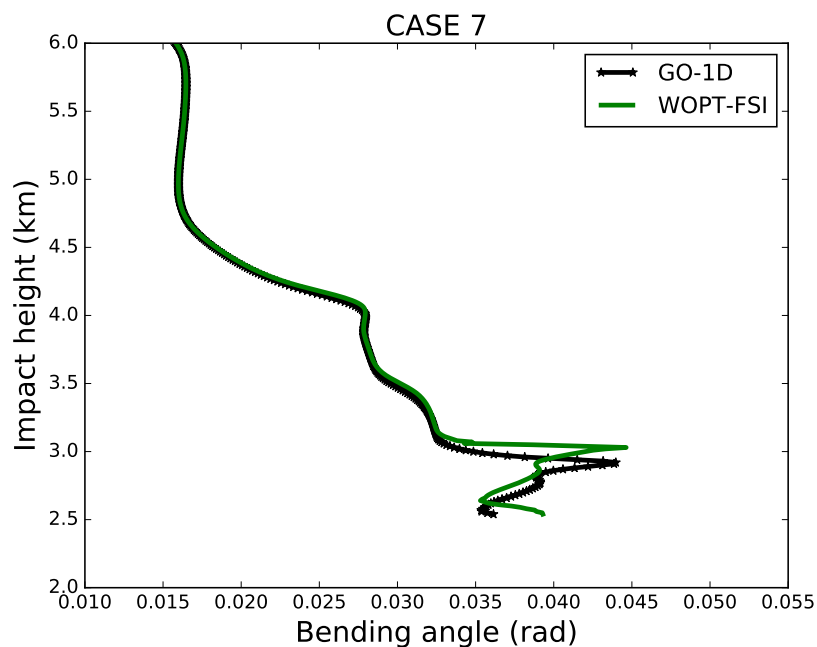


Figure 3.2: The retrieved bending angles produced with the wave optics propagator and FSI inverse (green line) and the one-dimensional geometrical optics simulation (black line) for the category 2 profile. See table 3.1.

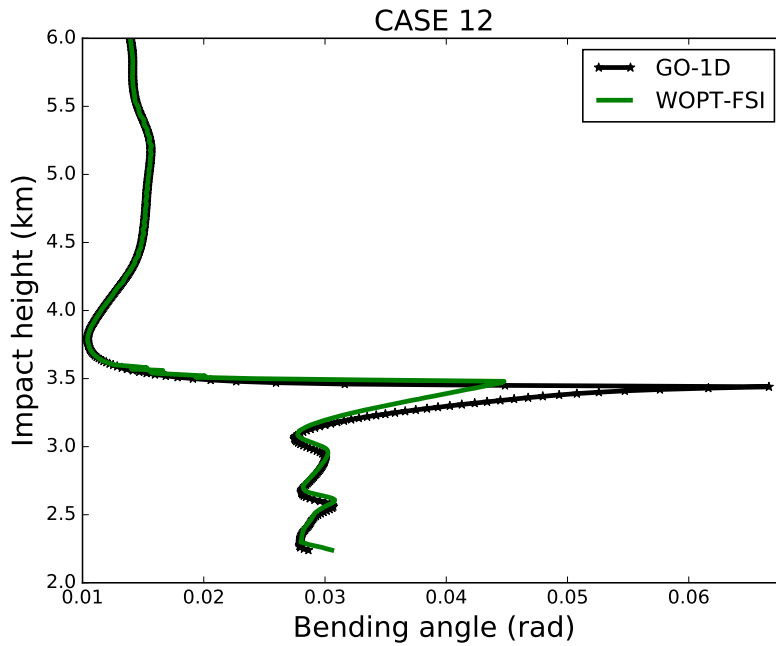


Figure 3.3: The retrieved bending angles produced with the wave optics propagator and FSI inverse (green line) and the one-dimensional geometrical optics simulation (black line) for the category 3 profile. See table 3.1.

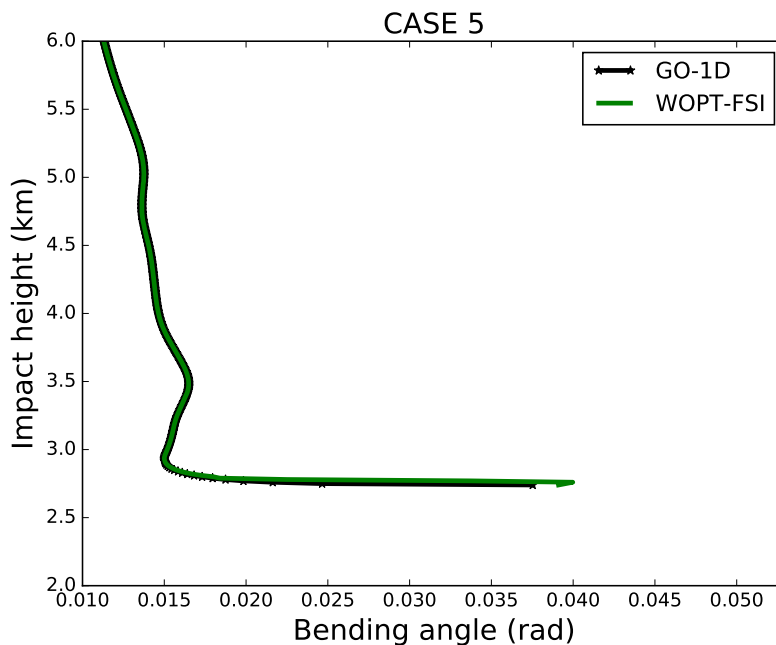


Figure 3.4: The retrieved bending angles produced with the wave optics propagator and FSI inverse (green line) and the one-dimensional geometrical optics simulation (black line) for the category 4 profile. See table 3.1.

3.2 Suggested modifications for ROPP-9.1

As noted above, simulations provided by Joel Rasch (Molflow, Sweden) for case 12 have led to a modification of the wave optics simulator for inclusion in ROPP-9.1. After significant testing, we found that a small modification to the propagation from the final screen to the LEO can improve the retrieved bending angles in the lowest few km, particularly when the bending angle is large.

In section 2.3, we approximate the exponent in Eq. 2.7 with $r \simeq x_r + \frac{(y-y_r)^2}{2x_r}$, and we show that this ultimately leads to a solution based on summing Fresnel integrals over a set of j vertical intervals, $\mathbf{U}(x_r, y_r) = \sum_j \delta \mathbf{U}_j$, where \mathbf{U}_j is given by Eq. 2.24. The next term in the expansion for r is,

$$r \simeq x_r + \frac{(y-y_r)^2}{2x_r} - \frac{(y-y_r)^4}{8x_r^3}. \quad (3.2)$$

In large bending angle cases, we have found that the errors in the lowest 2 km can be reduced by approximating this extra term in the exponent of Eq. 2.10.

We can improve the solution given in section 2.3 in the following way. Given \mathbf{U}_j evaluated with Eq. 2.24 we introduce an additional phase factor in the final summation over the vertical intervals to give,

$$\mathbf{U}(x_r, y_r) = \sum_j \delta \mathbf{U}_j \times \exp\left(-i \frac{k}{8x_r^3} (y_m^j - y_r)^4\right) \quad (3.3)$$

where y_m^j is y co-ordinate in the middle of the j^{th} vertical interval. This approximation assumes that the additional phase factor does not vary significantly within a given vertical integration interval, but it can vary between intervals. We can estimate the variation of this phase factor over a $\Delta y = 32$ m vertical interval, assuming a large bending angle of 0.07 rad ($\sim (y-y_r)/x_r$) and a 0.2 m wavelength,

$$\Delta\phi \simeq \frac{k}{2} \left(\frac{y-y_r}{x_r}\right)^3 \Delta y = 0.17 \text{ rad} \quad (3.4)$$

noting that this term scales as bending angle to the power 3.

The improvement on the bending angles produced in the wave optics simulations is shown in Figures 3.5 to 3.8. The results with the ROPP-9 implementation are also shown for reference. The proposed ROPP-9.1 implementation clearly corrects the wave optics bending angle errors in both Figure 3.6 and Figure 3.7.

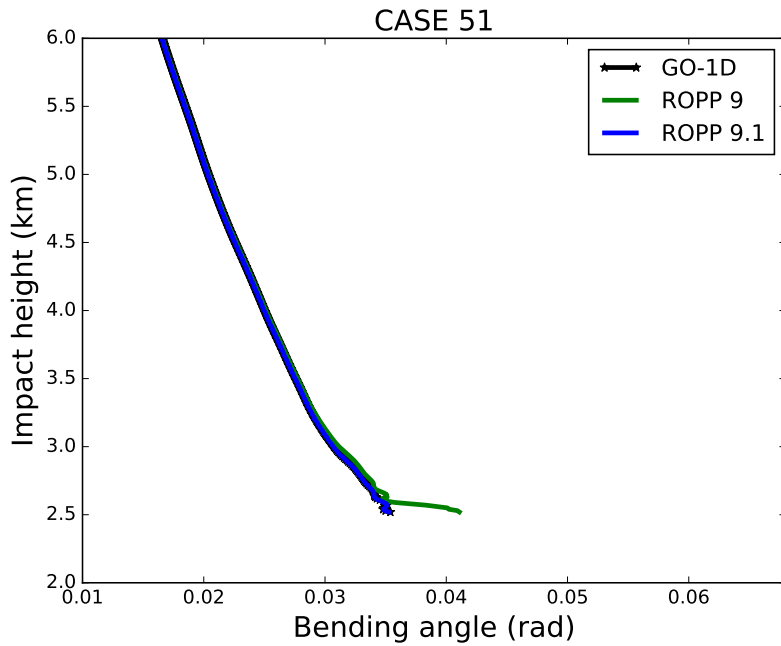


Figure 3.5: The retrieved bending angles produced with the wave optics propagator and FSI inverse for ROPP 9 (green line), ROPP 9.1 (blue line) and the one-dimensional geometrical optics simulation (black line) for the category 1 profile.

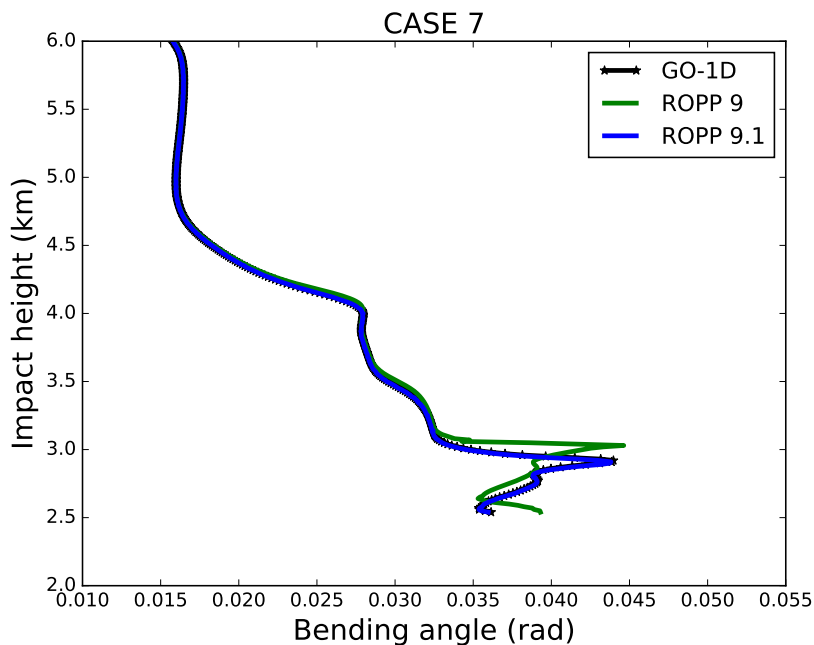


Figure 3.6: The retrieved bending angles produced with the wave optics propagator and FSI inverse for ROPP 9 (green line), ROPP 9.1 (blue line) and the one-dimensional geometrical optics simulation (black line) for the category 2 profile.

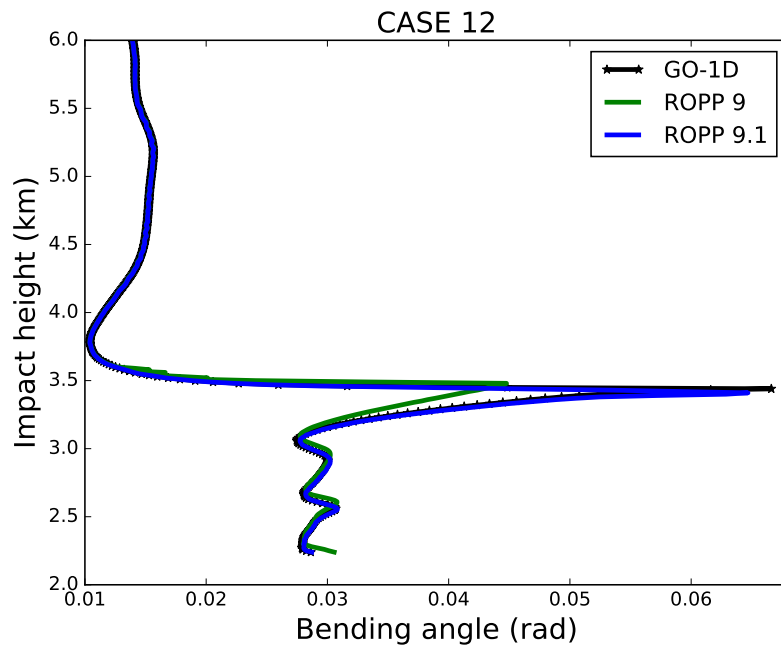


Figure 3.7: The retrieved bending angles produced with the wave optics propagator and FSI inverse for ROPP 9 (green line), ROPP 9.1 (blue line) and the one-dimensional geometrical optics simulation (black line) for the category 3 profile.

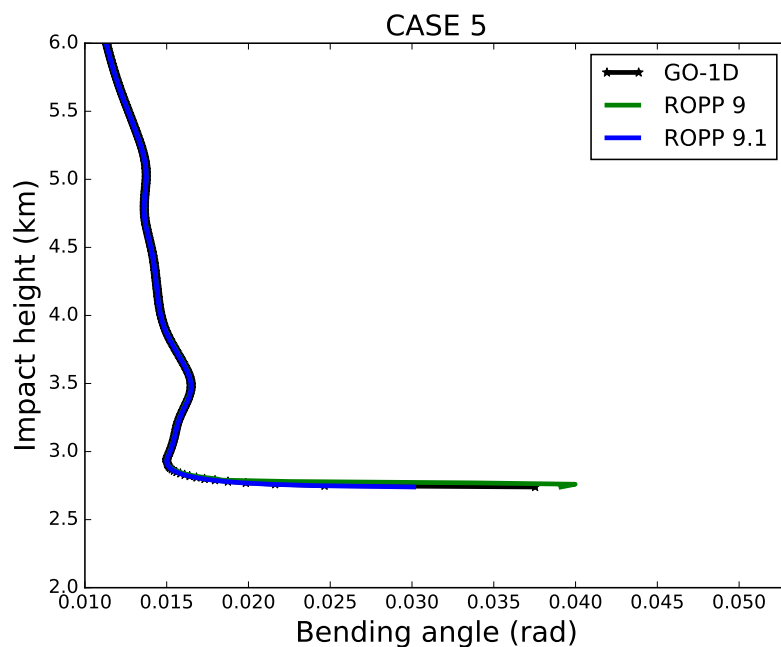


Figure 3.8: The retrieved bending angles produced with the wave optics propagator and FSI inverse for ROPP 9 (green line), ROPP 9.1 (blue line) and the one-dimensional geometrical optics simulation (black line) for the category 4 profile.

4 Summary

This report outlines the physical basis the wave optics simulation code available in ROPP 9. The code is based on the standard MPS approach which has been used previously (e.g., Karayel and Hinson, 1997; Sokolovskiy, 2001). The approach for propagating from the final phase screen to the LEO is novel, and it has been shown that this computation can be performed by summing standard Fresnel integrals. Some errors for large bending angles in the lowest 2 km have been identified for the ROPP-9 code, and a simple modification for ROPP-9.1 has been developed and tested.

ROPP-9 users can contact S. B. Healy (sean.healy@ecmwf.int) directly for more information relating to the ROPP-9.1 changes.

Acknowledgments

I would like to thank Joel Rasch (Molflow, Sweden) for important discussions relating to ROPP 9.1. Many thanks to Ian Culverwell for reviewing the report, and checking section 2.3.

References

- Abramowitz, M., and I. A. Stegun, 1972: *Mathematical functions with formulas, graphs, and mathematical tables*. Dover Publications, New York.
- Goodman, J. W., 1996: *Introduction to Fourier Optics*. McGraw-Hill, International Editions.
- Gorbunov, M. E., 2011: Wave optics propagator package: Description and user guide. Technical Report for contract EUM/co/10/460000812/CJA order 4500005632, EUMETSAT, Darmstadt, Germany.
- Gorbunov, M. E., and K. B. Lauritsen, 2007: Linearized Zverev Transform and its application for modeling radio occultations. *Radio Sci.*, **42**, RS3023, doi:10.1029/2006RS003590.
- Heald, M. A., 1985: Rational Approximations for the Fresnel Integrals. *Mathematics of Computation*, **44**, 459–461.
- Jensen, A., M. Lohmann, H.-H. Benzon, and A. Nielsen, 2003: Full Spectrum Inversion of radio occultation signals. *Radio Sci.*, **38**, 1040, doi:10.1029/2002RS002763.
- Karayel, E., and D. Hinson, 1997: Sub-Fresnel-scale vertical resolution in atmospheric profiles from radio occultation. *Radio Sci.*, **32**, 411–423.
- Press, W., S. Teukolsky, W. Vetterling, and B. Flannery, 1992: *Numerical recipes in Fortran – The art of scientific computing*, 2nd ed. Cambridge University Press, Cambridge, New York.
- Sokolovskiy, S. V., 2001: Modeling and inverting radio occultation signals in the moist troposphere. *Radio Sci.*, **36**, 441–458.
- Sokolovskiy, S. V., W. Schreiner, Z. Zeng, D. Hunt, Y.-C. Lin, and Y.-H. Kuo, 2014: Observation, analysis, and modeling of deep radio occultation signals: Effects of tropospheric ducts and interfering signals. *Radio Sci.*, **49**, 954–970, doi:10.1002/2014RS005436.

ROM SAF (and GRAS SAF) Reports

| | |
|---------------------------|---|
| SAF/GRAS/METO/REP/GSR/001 | Mono-dimensional thinning for GPS Radio Occultation |
| SAF/GRAS/METO/REP/GSR/002 | Geodesy calculations in ROPP |
| SAF/GRAS/METO/REP/GSR/003 | ROPP minimiser - minROPP |
| SAF/GRAS/METO/REP/GSR/004 | Error function calculation in ROPP |
| SAF/GRAS/METO/REP/GSR/005 | Refractivity calculations in ROPP |
| SAF/GRAS/METO/REP/GSR/006 | Levenberg-Marquardt minimisation in ROPP |
| SAF/GRAS/METO/REP/GSR/007 | Abel integral calculations in ROPP |
| SAF/GRAS/METO/REP/GSR/008 | ROPP thinner algorithm |
| SAF/GRAS/METO/REP/GSR/009 | Refractivity coefficients used in the assimilation of GPS radio occultation measurements |
| SAF/GRAS/METO/REP/GSR/010 | Latitudinal Binning and Area-Weighted Averaging of Irregularly Distributed Radio Occultation Data |
| SAF/GRAS/METO/REP/GSR/011 | ROPP 1dVar validation |
| SAF/GRAS/METO/REP/GSR/012 | Assimilation of Global Positioning System Radio Occultation Data in the ECMWF ERA-Interim Re-analysis |
| SAF/GRAS/METO/REP/GSR/013 | ROPP PP validation |
| SAF/ROM/METO/REP/RSR/014 | A review of the geodesy calculations in ROPP |
| SAF/ROM/METO/REP/RSR/015 | Improvements to the ROPP refractivity and bending angle operators |
| SAF/ROM/METO/REP/RSR/016 | Simplifying EGM96 Undulation calculations in ROPP |
| SAF/ROM/METO/REP/RSR/017 | Simulation of L1 and L2 bending angles with a model ionosphere |
| SAF/ROM/METO/REP/RSR/018 | Single Frequency Radio Occultation Retrievals: Impact on Numerical Weather Prediction |
| SAF/ROM/METO/REP/RSR/019 | Implementation of the ROPP two-dimensional bending angle observation operator in an NWP system |
| SAF/ROM/METO/REP/RSR/020 | Interpolation artefact in ECMWF monthly standard deviation plots |
| SAF/ROM/METO/REP/RSR/021 | 5th ROM SAF User Workshop on Applications of GPS radio occultation measurements |
| SAF/ROM/METO/REP/RSR/022 | The use of the GPS radio occultation reflection flag for NWP applications |
| SAF/ROM/METO/REP/RSR/023 | Assessment of a potential reflection flag product |
| SAF/ROM/METO/REP/RSR/024 | The calculation of planetary boundary layer heights in ROPP |
| SAF/ROM/METO/REP/RSR/025 | Survey on user requirements for ionospheric products |
| SAF/ROM/METO/REP/RSR/026 | Estimates of GNSS radio occultation bending angle and refractivity error statistics |
| SAF/ROM/METO/REP/RSR/027 | Recent forecast impact experiments with GPS radio occultation measurements |
| SAF/ROM/METO/REP/RSR/029 | Testing reprocessed GPS radio occultation datasets in a reanalysis system |

ROM SAF Reports are accessible via the ROM SAF website: <http://www.romsaf.org>